Chapter 3

Characterization of sources with arbitrary coherence

This chapter introduces an innovative experimental method for the precise measurement of the 2×2 cross-spectral density (CSD) matrix, a critical tool for characterizing the coherence and polarization properties of incoherent vector light sources. The proposed technique enables a comprehensive analysis of the interaction between polarization and coherence by utilizing the CSD matrix framework. The developed approach is subsequently employed to investigate the influence of tailoring polarization states on a far-field coherence. This work establishes a robust foundation for understanding and controlling the interplay of coherence and polarization in complex optical systems.

3.1 Introduction

Spatial coherence, one of the fundamental properties of light, is the description of the statistical correlation between fields at a pair of spatial points [134]. With growing interest in low-coherence sources, numerous techniques for the measurement of two-point spatial coherence have been proposed. These include Young's pinhole interferometer [136-142], wavefront folding interferometer [143-148], Sagnac interferometer [154-158], multiple apertures [150-152], nanoscatterers [165], coherence holography [167-169], etc.

Scalar coherence theory effectively describes optical fields with uniform polarization states, but it falls short for fields that exhibit partial coherence and varying polarization. Such fields, characterized as electromagnetic or vectorial optical fields, encompass components with distinct coherence and polarization properties [2, 134, 180]. Joint effect of polarization and coherence plays a critical role in the characterization of stochastic vector fields and in advanced imaging. These fields exhibit the influence of coherence and polarization, where different field components may show varying coherence properties [2]. The coherence and polarization characteristics of such fields have been observed to be inherently intertwined [236, 237]. For a complete explanation of the statistical properties of these random vectorial light fields, the electromagnetic coherence theory is thoroughly developed [2, 236, 237]. In the space-frequency domain, the central quantity to characterize the vectorial light fields is a 2x2 cross-spectral density (CSD) matrix, having four elements. The CSD matrix provided the solutions to numerous unresolved problems in the optics [238, 239]. These fields have found a wide range of applications in optical imaging [240], super-resolution imaging [241], optical trapping [242], classification of biological samples [243], microscopy [244, 245], surface plasmon structuring [246], etc. These properties arise because of the extensive tailoring potential of these vectorial fields, offering precise control over beam shape, polarization, and coherence not only at the source plane but also in other

regions. Many attempts have been made to synthesize vectorial coherence including electromagnetic Gaussian-Schell model sources [247, 248], special correlation functions [249], and vectorial coherence holography [198]. Different techniques have been developed to tailor and examine vectorial coherence using liquid crystal spatial light modulators [250-253]. A complete access and adaptive control over the orthogonal polarization components of light helps in creating the desired vectorial coherence.

To access and analyze the coherence structures, it is important to experimentally measure the vectorial coherence which is not a directly observable quantity like the intensity. The visibility of the intensity fringes in Young's two-pinhole interference experiment has historically been used to measure the coherence of light [134]. Similar approach is also extended to the polarization domain to characterize the vector light field [194-196]. Although Young's interferometer is conceptually simple, it possesses certain inherent limitations. The most prominent of these limitations is the low light efficiency of Young's two-pinhole setup, which poses challenges for characterizing weak light fields. As well as sequential scanning for point sampling is extremely time-consuming. Alternative methods relying on the concept of Young's approach have been developed to address some of these limitations [144, 254]. Another method based on the Hanbury Brown–Twiss (HBT) experiment is introduced for random vector light fields following Gaussian statistics. The method uses the intensity correlations to determine the amplitude of the two-point field correlation [255]. Later, our research group proposed a method to retrieve the complete information of the complex coherence function by adding a reference random light field and using the intensity correlation [203]. They also extended this approach for the vector source [185]. In another development, the concept of generalized HBT is introduced and experimental results are presented on the measurement of complex coherence functions of the scalar and vector light [206, 256]. Cai et al. have discussed and experimentally

demonstrated the synthesis and measurement of complex correlation matrix of the specially correlated radially polarized (SCRP) vector source [206]. This method involves combining the incoherent vector beam with a pair of fully coherent reference beams and analyzing the intensity-intensity cross-correlation of the recorded patterns. Recently, another alternative method is introduced for measuring the elements of the CSD matrix of the SCRP vector beam using self-referencing holography [208]. In this technique, a spatial light modulator introduces phase perturbations at a reference point set inside the regions of the test beam. The interaction between the light from the perturbed point and the overall plane leads to interference intensity patterns at the Fourier plane, which unveils the information about the CSD matrix elements. Also, methods based on using aperture diffraction and scattering through nanoparticles has been realized to measure vectorial coherence [202, 209]. Sourav et al. recently introduced a Folded interferometer to measure the CSD matrix, advancing experimental techniques for coherence analysis [210, 211]. The unified theory of coherence and polarization has provided a robust framework for innovative holographic and imaging applications [257, 258]. To extend these methods for vectorial incoherent sources, designing experimental setups capable of extracting the CSD matrix elements is crucial for further development in this domain.

In this chapter, we present a novel technique for two-dimensional measurement of the CSD matrix and recording of incoherent holograms of the vector object using the spatial complex coherence of the light. To experimentally measure the CSD matrix we propose a modified Sagnac radial shearing interferometer. Combination of radial shearing with the phase-shifting approach helps to retrieve the complex elements of the CSD matrix. Experimental implementation of our technique is in two parts. The first part deals with the illumination of an incoherent vector object by a yellow light-emitting diode (LED) and the incoherent vector object is encoded into the far-field elements of the 2x2 CSD matrix and a common

path Sagnac cyclic radial shearing interferometer. Second part introduces the phase-shifts in the interferogram to extract the complex elements of the CSD matrix. Experimentally measured CSD matrix elements are digitally back-propagated to recover the incoherent vector object. We have also shown the propagation of recorded vector source matrix elements at different distances with the help of the CSD matrix elements. Due to the propagation property of the complex coherence, it can be further used to reconstruct a 3D vector object. The interferometer offers to demonstrate the application of the CSD matrix elements in the recording of incoherent vector holograms. Later, we applied this developed technique to study effect of different polarization features such as unpolarized, diagonally polarized, and spatially depolarized on the CSD matrix element.

3.2 Measurement of cross-spectral density matrix

3.2.1 Theoretical basis

Consider an incoherently illuminated object placed at a transverse plane $z = 0$. The two arbitrary field points located at its cross-section are represented by position vectors $\mathbf{v}_1$ and $\mathbf{v}_2$. The second-order vector correlation property of the stochastic light field emerging from the object can be characterized by the CSD matrix [2]. The CSD matrix is expressed as

$$\mathbf{W}(\mathbf{v}_1, \mathbf{v}_2;\, \omega) = \begin{pmatrix} W_{xx}(\mathbf{v}_1, \mathbf{v}_2;\, \omega) & W_{xy}(\mathbf{v}_1, \mathbf{v}_2;\, \omega) \\ W_{yx}(\mathbf{v}_1, \mathbf{v}_2;\, \omega) & W_{yy}(\mathbf{v}_1, \mathbf{v}_2;\, \omega) \end{pmatrix} \tag{3.1}$$

where $$W_{sq}(\mathbf{v}_1, \mathbf{v}_2;\, \omega) = \langle U_s^*(\mathbf{v}_1;\, \omega) U_q(\mathbf{v}_2;\, \omega) \rangle \tag{3.2}$$

where $(s, q) \equiv (x, y)$, $U_x(\mathbf{v};\, \omega)$ and $U_y(\mathbf{v};\, \omega)$ are the stochastic field components along the x and y directions, respectively and ω is the frequency of the source. The asterisk denotes the complex conjugate and the angular bracket denotes the ensemble average.

The elements of the CSD matrix are expressed as the integral of the form [259]

$$W_{sq}(\boldsymbol{r}_1, \boldsymbol{r}_2;\ \omega) = \iint W_{sq}(\mathbf{v}_1, \mathbf{v}_2;\ \omega) H^*(\boldsymbol{r}_1, \mathbf{v}_1) H(\boldsymbol{r}_2, \mathbf{v}_2) d^2\mathrm{v}_1 d^2\mathrm{v}_2 \tag{3.3}$$

where, $W_{sq}(\mathbf{v}_1, \mathbf{v}_2)$ and $W_{sq}(\boldsymbol{r}_1, \boldsymbol{r}_2)$ corresponds to the input and output plane CSD matrix respectively, $\mathbf{v}$ is coordinate at the Fourier plane as represented in Fig. 3.1. $H(\boldsymbol{r}, \mathbf{v})$ is an arbitrary kernel connecting the two transverse planes in the free space.

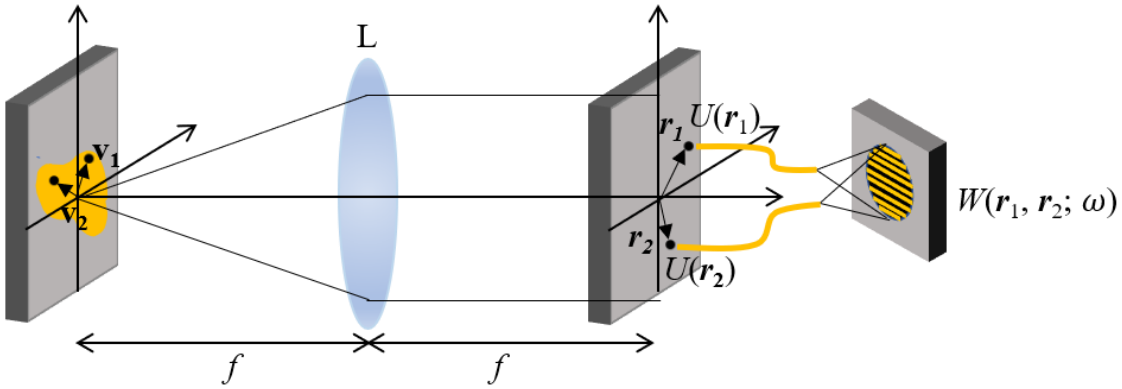

Fig. 3.1 Recording of incoherent object hologram by the CSD.

For a spatially incoherent vector source, any two points of the source are mutually uncorrelated and the source correlation function is represented using 2D delta function as

$$W_{sq}(\mathbf{v}_1, \mathbf{v}_2;\ \omega) = \sqrt{I_{sq}(\mathbf{v}_1;\ \omega) I_{sq}(\mathbf{v}_2;\ \omega)}\, \delta_{sq}(\mathbf{v}_2 - \mathbf{v}_1) \tag{3.4}$$

Therefore, Eq. 3.3 transforms to

$$W_{sq}(\boldsymbol{r}_1, \boldsymbol{r}_2;\ \omega) = \int I_{sq}(\mathbf{v};\ \omega) H^*(\boldsymbol{r}_1, \mathbf{v}) H(\boldsymbol{r}_2, \mathbf{v}) d^2\mathbf{v} \tag{3.5}$$

where $I_{sq}(\mathbf{v};\ \omega)$ are the elements of a 2x2 matrix representing polarization by single-point correlation. The diagonal elements of the matrix $I_{sq}(\mathbf{v};\ \omega)$ are real for $s = q$, and off-diagonal elements of the matrix $I_{sq}(\mathbf{v};\ \omega)$ may take complex values for $s \neq q$.

For a Fourier propagation, the propagation kernel is represented as

$$H(\boldsymbol{r}, \mathbf{v}) = \exp\left(-i2\pi(\mathbf{v}.\boldsymbol{r})\right) \tag{3.6}$$

On substituting Eq. (3.6) into Eq. (3.5), the elements of the CSD matrix at the output plane is represented as

$$W_{sq}(\boldsymbol{r}_1, \boldsymbol{r}_2;\ \omega) = \int I_{sq}(\mathbf{v};\ \omega) \exp[-i2\pi \mathbf{v}.(\boldsymbol{r}_2 - \boldsymbol{r}_1)]\, d^2\mathbf{v} \tag{3.7}$$

Eq. (3.7) represents the vectorial van Cittert-Zernike theorem depending on the difference of coordinates $\boldsymbol{r}_2 - \boldsymbol{r}_1$ [199, 201]. Eq. (3.7) connects the incoherent vector source with the elements of the CSD matrix through a Fourier transforms relation. To experimentally determine the elements of the CSD matrix, a suitable interferometer is developed as discussed in the next section.

3.2.2 Experiment and results discussions

In order to experimentally record and reconstruct the incoherent vector holograms, we devised our experimental strategy into two parts. Part I covers recording of incoherent vector hologram and a common-path radial shearing cyclic interferometer for measurement of the coherence function. Part II covers part of the experimental setup to introduce phase shifts in the interfering beams for extraction of the complex coherence function from the fringes. The stochastic field at the Fourier plane as shown by the dotted blue line in Fig. 3.2 is directed to the interferometer and imaged at the detector plane. The cyclic interferometer is designed with a telescopic lens system composed of lenses L2 and L3 which introduces an in-plane radial shear $\Delta\boldsymbol{r}$ between the counter-propagating beams with magnifications α and α^{-1}, respectively. The coordinates at the Fourier plane are now scaled according to the scaling parameter α, $\boldsymbol{r}_2 = \alpha\boldsymbol{r}$ and $\boldsymbol{r}_1 = \alpha^{-1}\boldsymbol{r}$. Therefore, we get two-point correlation of the fields between variable points $\Delta\boldsymbol{r} = (\alpha - \alpha^{-1})\boldsymbol{r}$ at the image plane. The elements of the CSD matrix $W_{sq}(\boldsymbol{r}_1, \boldsymbol{r}_2;\ \omega)$ are now scaled as $W_{sq}(\alpha^{-1}\boldsymbol{r}, \alpha\boldsymbol{r},;\ \omega)$. The experimental sketch is shown in Fig. 3.2 and a detailed explanation is given below.

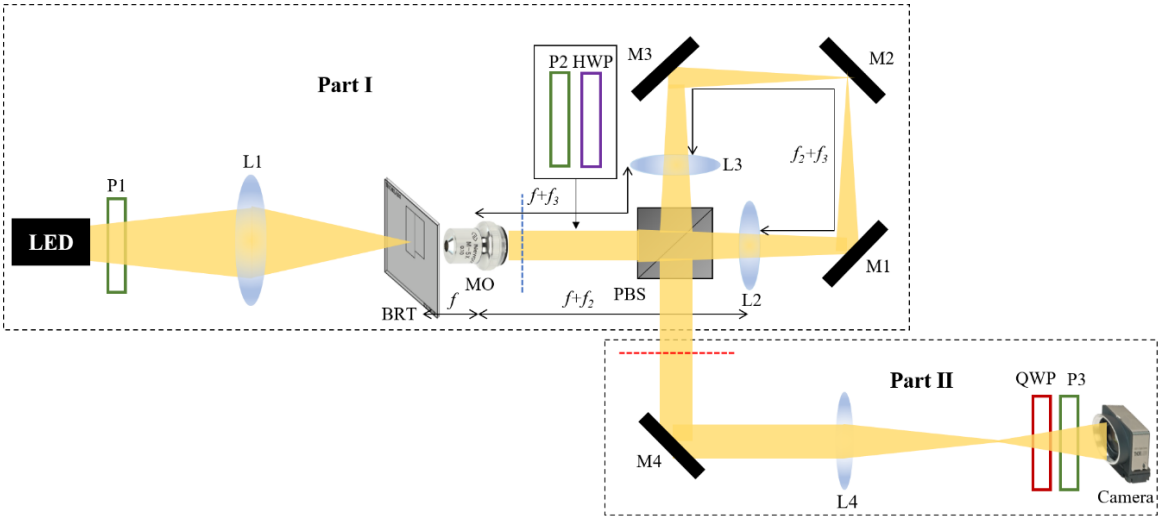

Fig. 3.2 Experimental set up: P, Polarizer; L, Lens; BRT, Birefringent Resolution Target; MO, Microscopic Objective; PBS, Polarization Beam Splitter; M, Mirror; HWP, Half Wave Plate; QWP, Quarter Wave Plate.

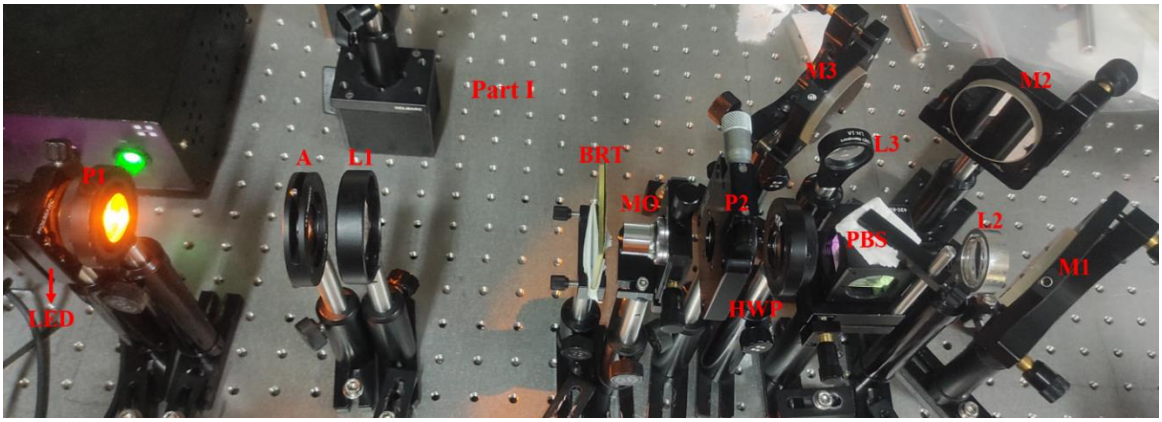

Fig. 3.3 Laboratory experimental setup.

Fig. 3.2 shows the experimental design, where the lens L1 with focal length f_1 = 60 mm is kept after a yellow light LED such that it will image the LED onto the object. Here object is selected from the transparent birefringent resolution target (BRT) chart. The BRT is a birefringent NBS 1963 US resolution target (Thorlabs: R2L2S1B) and the number '6' of this target is illuminated by the incoherent light from the LED. A Fourier transform of this incoherently illuminated object exists at the back focal plane of a microscopic objective (MO) with focal length f = 25.4 mm, and this plane is represented by the blue dotted line. The coherence distribution of the vector incoherent source is shaped according to the van

Cittert-Zernike theorem and the complex coherence distribution at the Fourier plane is experimentally measured by the Sagnac interferometer. Now, the stochastic field is directed into the square Sagnac cyclic interferometer comprising of polarizing beam splitter (PBS), mirror system (M1, M2, and M3) and telescopic lens system (L2 and L3). The PBS divides the field into two orthogonal polarization components and the telescopic lens system L2 and L3 with focal lengths f_2 = 120 mm and f_3 = 125 mm gives a radial shear between the two counter-propagating beams with magnifications $\alpha = f_3/f_2 = 1.041$ and $\alpha^{-1} = f_2/f_3 = 0.96$, respectively. The two radially sheared copies of the fields at the image plane of the telescopic system, represented by the red dotted line, are small in size. Therefore, a magnifying lens L4 with focal length f_4 = 150 mm is used to magnify the image and record the interference pattern at the CMOS camera (Thorlabs DCC3240M with pixel size 5.3μm). A tilt is introduced in the two counter-propagating beams by mirror M2 to make off-axis interference fringes as shown below in the experimental results of the fringes. Fig. 3.3 shows a laboratory picture of the experimental set up.

To measure the complex element of the CSD matrix, a combination of quarter wave plate (QWP) and polarizer (P3) is introduced before the camera to introduce the geometric phase shift and record the phase-shifted interferograms as shown in Part II of Fig. 3.2. As our interferometer is a common path interferometer it's not possible to introduce the dynamical phase shift. Therefore, instead of introducing dynamic phase shift we will introduce geometrical phase shift. In 1955, Pancharatnam demonstrated that when the polarization state of light undergoes a cyclic transformation, the associated phase change is determined solely by the geometric properties of the trajectory traced on the Poincaré sphere [175, 176]. This geometric phase, later explored in detail by Berry (1987), highlights the intrinsic connection between polarization transformations and the underlying geometry of the light's state space [177, 260]. In general, the geometric phase arises when the state of a system

undergoes a cyclic evolution, meaning it returns to its original state after traversing a closed trajectory. For such cases, the geometric phase corresponds to half the solid angle subtended by the closed path on the Poincaré sphere [261]. However, this concept extends to noncyclic evolutions as well. When the evolution path is not closed, the geometric phase can still be determined by employing the geodesic rule, where the open ends of the trajectory are connected by geodesic segments to complete the curve [262, 263]. One such design with unclosed paths is shown in Fig. 3.4. A practical type of retarder with such geometry involves the use of a quarter-wave plate (QWP) to transform linear polarization into circular polarization, followed by a polarizer (P3) to project this circularly polarized light into a linearly polarized state through a non-unitary process [264]. The beams pass through a QWP, whose fast axis is oriented at $\pi/4$ to the polarization directions. This process shifts the orthogonal linear polarization states of the beams along distinct paths on the Poincaré sphere to right-handed and left-handed circular polarization (RCP and LCP), represented as points C and D. A polarizer P3, rotated by an angle θ relative to the x-axis, projects these beams onto a new state E on the sphere. The geometric phase of each beam is determined by connecting their initial states B and B' to the projected state E via imaginary geodesics. Consequently, the introduced phase difference between the beams is 2θ. By varying θ, it becomes possible to shift the interference fringes in the resulting pattern. Consider the RCP and LCP beams with amplitudes denoted as $a_s(\boldsymbol{r}_1)$ and $a_q(\boldsymbol{r}_2)$, and phases represented by $\phi_s(\boldsymbol{r}_1)$ and $\phi_q(\boldsymbol{r}_2)$, respectively. Using the Jones vectors representation, the fields emerging out of QWP are expressed as [265]

$$U_s(\boldsymbol{r}_1) = \begin{pmatrix} 1 \\ i \end{pmatrix} a_s(\boldsymbol{r}_1)\, exp\big(i\phi_s(\boldsymbol{r}_1)\big), \quad \text{(RCP)} \tag{3.8}$$

and

$$U_q(\boldsymbol{r}_2) = \begin{pmatrix} 1 \\ -i \end{pmatrix} a_q(\boldsymbol{r}_2)\, exp\left(i\phi_q(\boldsymbol{r}_2)\right), \quad \text{(LCP)} \tag{3.9}$$

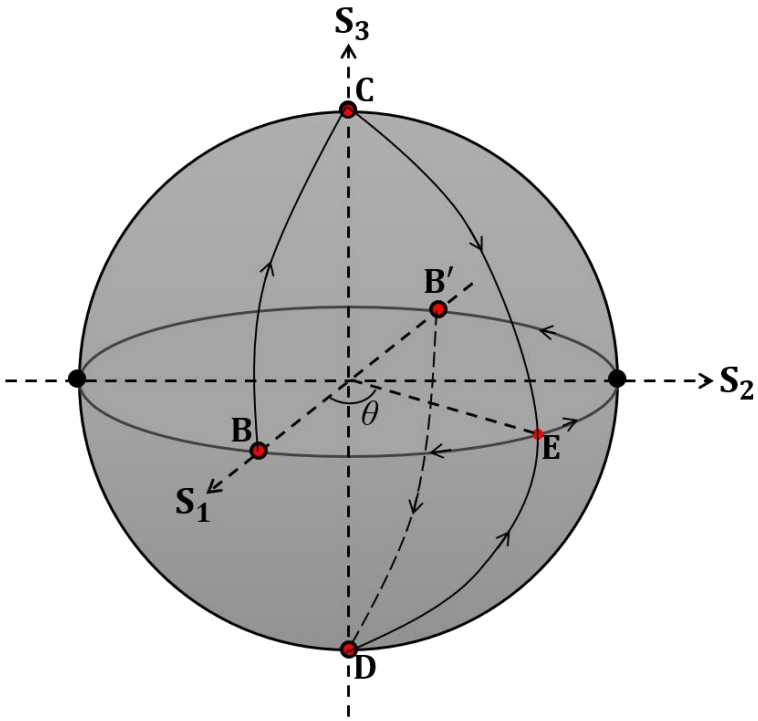

Fig. 3.4 Polarization-state trajectories on the Poincaré sphere.

Following the QWP, the polarizer P3 is positioned at an angle θ relative to the x-axis. The Jones matrix related to the polarizer is [265]

$$P(\theta) = \begin{bmatrix} cos^2\,\theta & sin\theta\,cos\theta \\ sin\theta\,cos\theta & sin^2\,\theta \end{bmatrix}, \tag{3.10}$$

Therefore, the horizontal and vertical components of the field transmitted by the polarizer are represented as

$$\begin{bmatrix} U_x(\boldsymbol{r}_1) \\ U_y(\boldsymbol{r}_2) \end{bmatrix} \propto \begin{bmatrix} cos^2\,\theta & sin\theta\,cos\theta \\ sin\theta\,cos\theta & sin^2\,\theta \end{bmatrix} \left(\begin{bmatrix} 1 \\ i \end{bmatrix} a_s(\boldsymbol{r}_1)\, exp\big(i\phi_s(\boldsymbol{r}_1)\big) + \right.$$

$$\left. \begin{bmatrix} 1 \\ -i \end{bmatrix} a_q(\boldsymbol{r}_2)\, exp\left(i\phi_q(\boldsymbol{r}_2)\right) \right), \tag{3.11}$$

$$\begin{bmatrix} U_x(\boldsymbol{r}_1) \\ U_y(\boldsymbol{r}_2) \end{bmatrix} \propto \begin{bmatrix} cos\theta \\ sin\theta \end{bmatrix} \left(exp(i\theta)\, a_s(\boldsymbol{r}_1)\, exp\big(i\phi_s(\boldsymbol{r}_1)\big) + exp(-i\theta)\, a_q(\boldsymbol{r}_2)\, exp\left(i\phi_q(\boldsymbol{r}_2)\right) \right), \tag{3.12}$$

Equation (3.12) highlights that introducing a polarizer after the QWP projects the RCP and LCP fields at an angle θ with an additional phase offset of $+\theta$ and $-\theta$ in the components of the RCP and LCP fields, respectively.

Therefore, the average intensity at the detector plane as described by [2, 266]

$$I_{sq}(2\theta) \approx I_s(\boldsymbol{r}_1) + I_q(\boldsymbol{r}_2) + 2\sqrt{I_s(\boldsymbol{r}_1)}\sqrt{I_q(\boldsymbol{r}_2)}g_{sq}(\boldsymbol{r}_1,\boldsymbol{r}_2)\, cos\big[\phi_{sq}(\boldsymbol{r}_1,\boldsymbol{r}_2) + 2\theta\big], \tag{3.13}$$

where $I_{sq}(2\theta)$ is the averaged intensity, $I_s(\boldsymbol{r}_1) = \langle|a_s(\boldsymbol{r}_1)|^2\rangle$ and $I_q(\boldsymbol{r}_2) = \langle\big|a_q(\boldsymbol{r}_2)\big|^2\rangle$. $g_{sq}(\boldsymbol{r}_1,\boldsymbol{r}_2)$ represents amplitude of the two-point correlation function and its argument is represented as $\phi_{sq}(\boldsymbol{r}_1,\boldsymbol{r}_2)$. Thus, rotating polarizer P3 introduces phase-shift 2θ into the interfering beams.

Considering $I_0 = I_s(\boldsymbol{r}_1) = I_q(\boldsymbol{r}_2)$, we express the intensity at the detector as

$$I_{sq}(2\theta) \approx I_0\left\{1 + g_{sq}(\boldsymbol{r}_1,\boldsymbol{r}_2)\, cos\big[\phi_{sq}(\boldsymbol{r}_1,\boldsymbol{r}_2) + 2\theta\big]\right\}, \tag{3.14}$$

Five interferograms with phase shifts 0, π/2, π, 3π/2 and 2π are recorded which are represented as

$$I_{sq}(0) \approx I_0\left\{1 + g_{sq}(\boldsymbol{r}_1,\boldsymbol{r}_2)\, cos\big[\phi_{sq}(\boldsymbol{r}_1,\boldsymbol{r}_2)\big]\right\}, \tag{3.15}$$

$$I_{sq}(\pi/2) \approx I_0\left\{1 + g_{sq}(\boldsymbol{r}_1,\boldsymbol{r}_2)\, cos\big[\phi_{sq}(\boldsymbol{r}_1,\boldsymbol{r}_2) + \pi/2\big]\right\}, \tag{3.16}$$

$$I_{sq}(\pi) \approx I_0\left\{1 + g_{sq}(\boldsymbol{r}_1,\boldsymbol{r}_2)\, cos\big[\phi_{sq}(\boldsymbol{r}_1,\boldsymbol{r}_2) + \pi\big]\right\}, \tag{3.17}$$

$$I_{sq}(3\pi/2) \approx I_0\left\{1 + g_{sq}(\boldsymbol{r}_1,\boldsymbol{r}_2)\, cos\big[\phi_{sq}(\boldsymbol{r}_1,\boldsymbol{r}_2) + 3\pi/2\big]\right\}, \tag{3.18}$$

$$I_{sq}(2\pi) \approx I_0\left\{1 + g_{sq}(\boldsymbol{r}_1,\boldsymbol{r}_2)\, cos\big[\phi_{sq}(\boldsymbol{r}_1,\boldsymbol{r}_2) + 2\pi\big]\right\}, \tag{3.19}$$

For a phase step β the fringe phase ϕ can be calculated using the formula [267]

$$\tan\phi_{sq}(\boldsymbol{r}_1,\boldsymbol{r}_2) = 2\sin\beta\,\frac{\big(I_{sq}(\pi/2) - I_{sq}(3\pi/2)\big)}{2I_{sq}(\pi) - I_{sq}(2\pi) - I_{sq}(0)} \tag{3.20}$$

where $I_{sq}(\phi)$ represents the recorded interferogram at a phase shift ϕ and β is defined as

$$\beta = \arccos\left[\frac{I_{sq}(0)-I_{sq}(2\pi)}{2\left(I_{sq}(\pi/2)-I_{sq}(3\pi/2)\right)}\right] \tag{3.21}$$

The fringe visibility g is given by [266]

$$g_{sq}(\boldsymbol{r}_1,\boldsymbol{r}_2) \propto \frac{\sqrt{\left[2\left(I_{sq}(0)-I_{sq}(3\pi/2)\right)\right]^2+\left(2I_{sq}(\pi)-I_{sq}(2\pi)-I_{sq}(0)\right)^2}}{I_{sq}(0)+I_{sq}(\pi/2)+I_{sq}(\pi)+I_{sq}(3\pi/2)+I_{sq}(2\pi)} \tag{3.22}$$

The five-phase shifted interferograms are recorded and the fringe phase and the fringe visibility are extracted using Eqs. (3.20), (3.21), and (3.22).

Thus, a complex CSD matrix element is represented by fringe visibility and fringe phase as

$$W_{sq}(\alpha^{-1}\boldsymbol{r},\alpha\boldsymbol{r}) = g_{sq}(\alpha^{-1}\boldsymbol{r},\alpha\boldsymbol{r})\, exp(i\phi_{sq}(\alpha^{-1}\boldsymbol{r},\alpha\boldsymbol{r})), \tag{3.23}$$

where $\alpha^{-1}\boldsymbol{r} = \boldsymbol{r}_1$ and $\alpha\boldsymbol{r} = \boldsymbol{r}_2$.

A polarizer P1 after the source helps to tune and filter the polarization properties of the LED and this polarizer is diagonally oriented in the experiment. Fig. 3.2 represents the experimental scheme to measure $W_{xy}(\alpha^{-1}\boldsymbol{r},\alpha\boldsymbol{r})$. As the incoming field is diagonally polarized, the orthogonal polarization components split into two counter-propagating beams by the PBS. A telescopic assembly in the Sagnac geometry introduces the radial shearing in the orthogonally polarized beams and interferogram is recorded at the camera plane by using projection of the orthogonal polarization components by P3. The experimentally recorded set of interferograms are used to digitally reconstruct $W_{xy}(\alpha^{-1}\boldsymbol{r},\alpha\boldsymbol{r})$. Fig. 3.5 (a)-(e) shows the five experimentally recorded interferograms for phase shifts 0, π/2, π, 3π/2 and 2π and the corresponding digitally constructed fringe visibility and the fringe phase of $W_{xy}(\alpha^{-1}\boldsymbol{r},\alpha\boldsymbol{r})$ as shown in Fig. 3.5 (f) and 3.5 (g),

respectively. The introduced phase shift changes the interference patterns of the recorded holograms as highlighted in Fig. 3.5 (a)-(e).

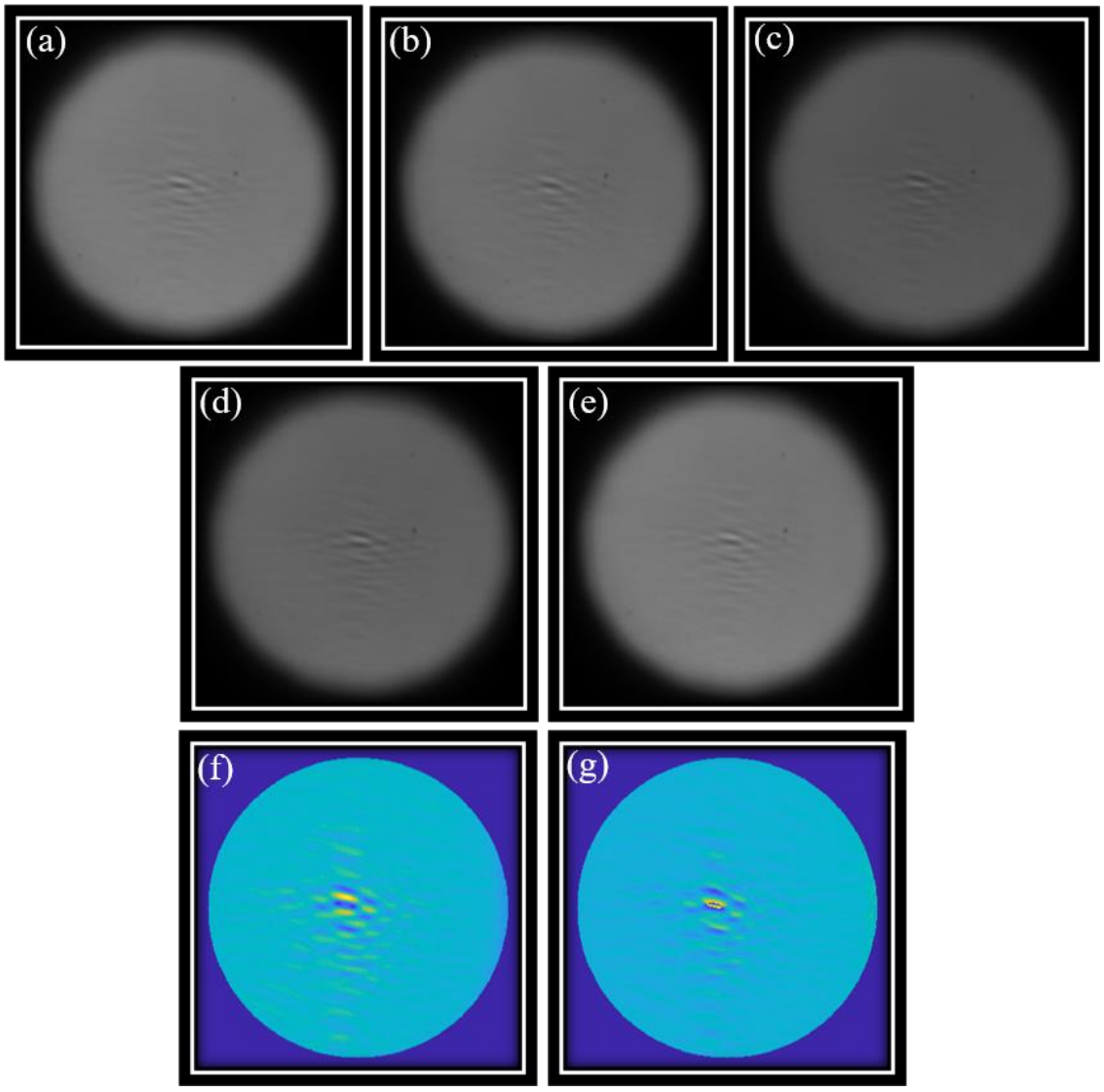

Fig. 3.5 Experimentally measured matrix element $\boldsymbol{W_{xy}(\alpha^{-1}r, \alpha r)}$ for polarized light: (a)-(e) Five experimentally recorded interferograms for phase shifts (a) 0 (b) π/2 (c) π (d) 3π/2 (e) 2π, and (f) constructed fringe visibility (g) corresponding phase.

In order to measure the diagonal element $W_{xx}(\alpha^{-1}\boldsymbol{r}, \alpha\boldsymbol{r})$**,** we insert optical components, polarizer P2 and half wave plate (HWP) in the experimental setup as shown in the inset in Fig. 3.2. The polarizer P2 is inserted and rotated to filter the x-polarized field from the stochastic source which is further diagonally rotated by a HWP oriented at 22.5˚ from its fast axis along the x direction. This strategy helps to make two counter propagating copies

by the PBS and a radial shearing by lens combination L2 and L3. These two fields interfere at the detector plane and make an interference pattern as explained previously. The experimentally recorded set of interferograms digitally reconstruct $W_{xx}(\alpha^{-1}\boldsymbol{r}, \alpha\boldsymbol{r})$.

In order to measure $W_{yy}(\alpha^{-1}\boldsymbol{r}, \alpha\boldsymbol{r})$**,** we filter a y-polarization component from the stochastic source using polarizer P2 and rotate it diagonally by the HWP. This field enters into the interferometer which makes two copies and generate set of interference patterns by a combination of QWP and polarizer P3 orientation. The experimentally recorded set of interferograms are used to digitally reconstruct $W_{yy}(\alpha^{-1}\boldsymbol{r}, \alpha\boldsymbol{r})$.

In order to experimentally measure $W_{yx}(\alpha^{-1}\boldsymbol{r}, \alpha\boldsymbol{r})$, we only insert the HWP oriented at 45˚ from its fast axis to flip the orientation of the polarization from x to y and y to x, respectively. This field enters into the interferometer and set of interferograms are recorded as discussed previously. These interferograms are used to digitally reconstruct $W_{yx}(\alpha^{-1}\boldsymbol{r}, \alpha\boldsymbol{r})$.

Fig. 3.6 shows all the experimentally measured CSD matrix elements for polarized light filtered from the LED. Fig. 3.6 (a)-(d) represents the digitally constructed fringe visibility and Fig. 3.6 (e)-(h) represents the corresponding phase of the CSD matrix elements. The off-diagonal elements of the CSD matrix show fringe visibility, and demonstrate a correlation between the cross-polarization components x and y. A correlation between the orthogonal polarization components emerges due to the polarization filtering of the LED light.

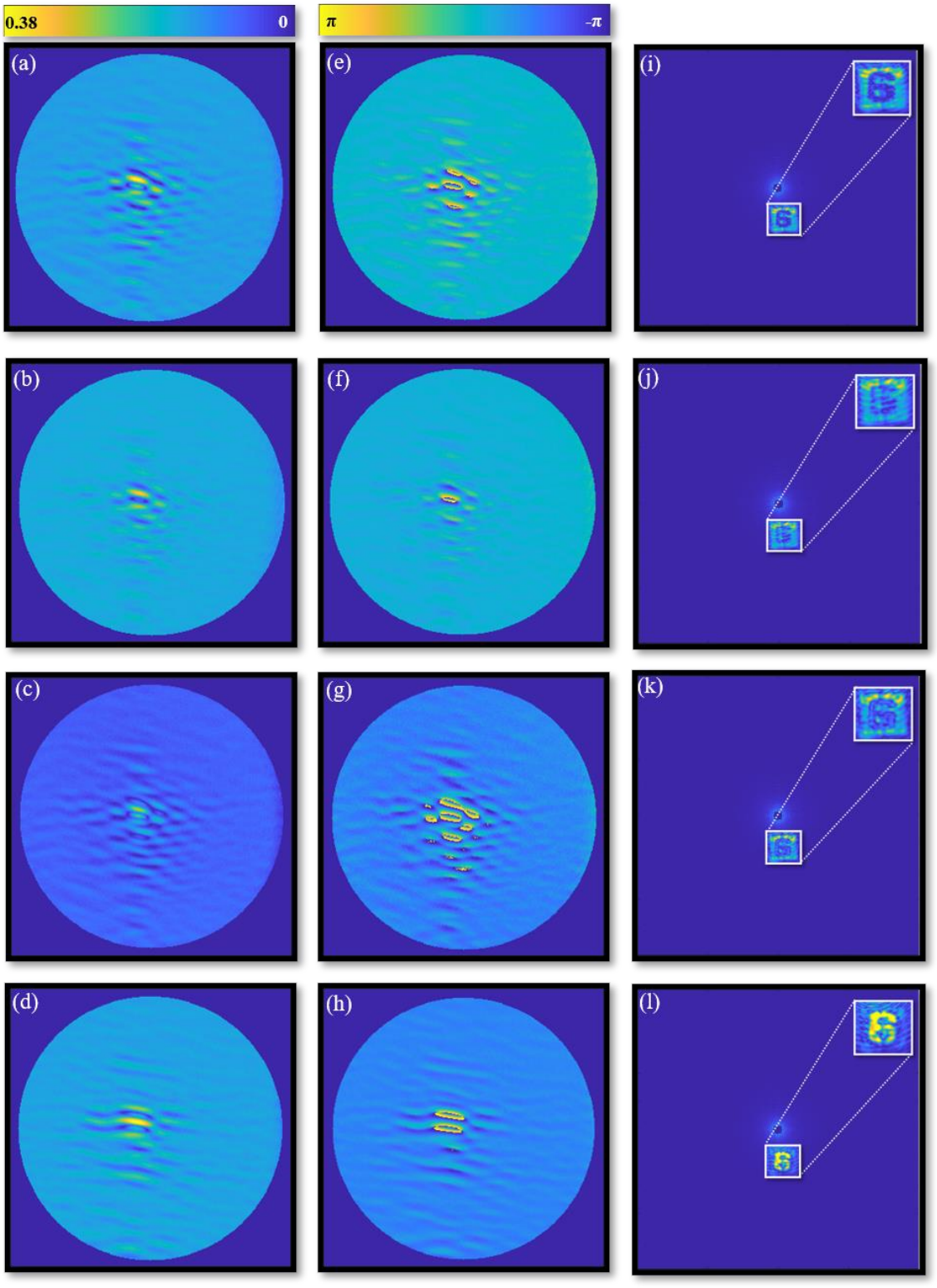

Fig. 3.6 Elements of cross-spectral density matrix for polarized light: fringe visibility of (a) $\boldsymbol{W_{xx}(\alpha^{-1}r, \alpha r)}$ (b) $\boldsymbol{W_{xy}(\alpha^{-1}r, \alpha r)}$ (c) $\boldsymbol{W_{yx}(\alpha^{-1}r, \alpha r)}$ (d) $\boldsymbol{W_{yy}(\alpha^{-1}r, \alpha r)}$, corresponding phase of (e) $\boldsymbol{W_{xx}(\alpha^{-1}r, \alpha r)}$ (f) $\boldsymbol{W_{xy}(\alpha^{-1}r, \alpha r)}$ (g) $\boldsymbol{W_{yx}(\alpha^{-1}r, \alpha r)}$ (h) $\boldsymbol{W_{yy}(\alpha^{-1}r, \alpha r)}$ and reconstructed vector source elements (i) $\boldsymbol{I_{xx}(r)}$ (j) $\boldsymbol{I_{xy}(r)}$ (k) $\boldsymbol{I_{yx}(r)}$ (l) $\boldsymbol{I_{yy}(r)}$ (colour bar shown above the Figs. (a)-(d) and Figs. (e)-(h) are same for all the Figs.)

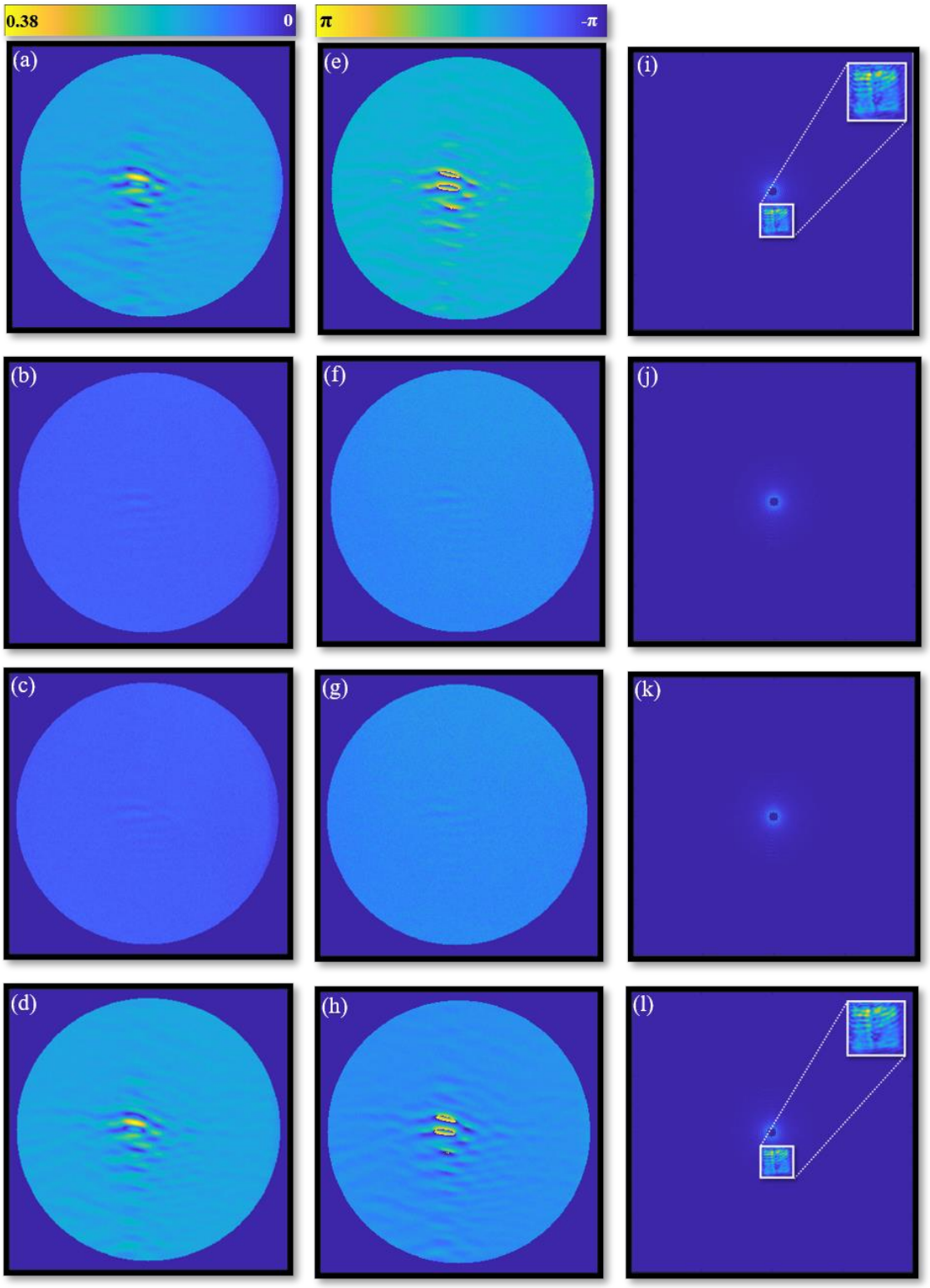

Fig. 3.7 Elements of cross-spectral density matrix for unpolarized light: fringe visibility of (a) $\boldsymbol{W_{xx}(\alpha^{-1}r, \alpha r)}$ (b) $\boldsymbol{W_{xy}(\alpha^{-1}r, \alpha r)}$ (c) $\boldsymbol{W_{yx}(\alpha^{-1}r, \alpha r)}$ (d) $\boldsymbol{W_{yy}(\alpha^{-1}r, \alpha r)}$, corresponding phase of (e) $\boldsymbol{W_{xx}(\alpha^{-1}r, \alpha r)}$ (f) $\boldsymbol{W_{xy}(\alpha^{-1}r, \alpha r)}$ (g) $\boldsymbol{W_{yx}(\alpha^{-1}r, \alpha r)}$ (h) $\boldsymbol{W_{yy}(\alpha^{-1}r, \alpha r)}$, reconstructed vector source elements (i) $\boldsymbol{I_{xx}(r)}$ (j) $\boldsymbol{I_{xy}(r)}$ (k) $\boldsymbol{I_{yx}(r)}$

(l) $\boldsymbol{I_{yy}(r)}$ (colour bar shown above the Figs. (a)-(d) and Figs. (e)-(h) are same for all the Figs.)

In order to test the inherent correlation features of the source, we removed the polarizer P1 from the experimental setup and measured all four elements of the CSD matrix as shown in Fig. 3.7. Fig. 3.7 (a)-(d) represents the digitally constructed fringe visibility and Fig. 3.7 (e)-(h) represents the corresponding phase for CSD matrix elements $W_{xx}(\alpha^{-1}\boldsymbol{r}, \alpha\boldsymbol{r})$, $W_{xy}(\alpha^{-1}\boldsymbol{r}, \alpha\boldsymbol{r})$, $W_{yx}(\alpha^{-1}\boldsymbol{r}, \alpha\boldsymbol{r})$ and $W_{yy}(\alpha^{-1}\boldsymbol{r}, \alpha\boldsymbol{r})$, respectively. The fringe visibility for off-diagonal elements of the CSD matrix as shown in Fig. 3.7 (b) and 3.7 (c), *i.e.*, $W_{xy}(\alpha^{-1}\boldsymbol{r}, \alpha\boldsymbol{r})$ and $W_{yx}(\alpha^{-1}\boldsymbol{r}, \alpha\boldsymbol{r})$ are zero which confirms the lack of correlations between the orthogonally polarized components and hence the LED source is incoherent and un-polarized. Whereas, Fig. 3.7 (a), (d), (e), and (h) shows the fringe visibility and phase of the diagonal elements, *i.e.*, $W_{xx}(\alpha^{-1}\boldsymbol{r}, \alpha\boldsymbol{r})$ and $W_{yy}(\alpha^{-1}\boldsymbol{r}, \alpha\boldsymbol{r})$.

Propagation of complex coherence and recovery of object

Our experimental scheme is capable to retrieve the 2D spatial structure of the complex correlation functions. The incoherent vector source is connected with the elements of the CSD matrix by the van Cittert-Zernike theorem as explained in Eq. (3.7). Furthermore, this relation can be used to digitally backpropagate the complex correlation functions and retrieve the source structure as

$$I'_{sq}(\mathbf{v};\ \omega) = \int W_{sq}(\alpha^{-1}\boldsymbol{r}, \alpha\boldsymbol{r};\ \omega)\exp[i2\pi(\alpha - \alpha^{-1})(\mathbf{v}.\boldsymbol{r})]\, d^2\boldsymbol{r} \qquad (3.24)$$

Fig. 3.6 **(**i)-(l) represents the vectorial source structures $I_{xx}(\boldsymbol{r})$, $I_{xy}(\boldsymbol{r})$, $I_{yx}(\boldsymbol{r})$ and $I_{yy}(\boldsymbol{r})$ for the polarized light using Eq. (3.24). Fig. 3.6 (i)-(l) shows the reconstructed objects, *i.e.*, a birefringent number "6" from different elements of the CSD matrix. Whereas, Fig. 3.7 (i)-(l) represents the reconstructed incoherent-vector source elements $I_{xx}(\boldsymbol{r})$, $I_{xy}(\boldsymbol{r})$, $I_{yx}(\boldsymbol{r})$ and $I_{yy}(\boldsymbol{r})$ respectively for the unpolarized light as explained previously in Fig. 3.7 (a)-(d).

On comparing results from the reconstructed source for the unpolarized and polarized light, Fig. 3.7 (i)-(l) show inherent features of the original illuminating source, i.e., LED and Fig. 3.7 (i)-(l) shows the reconstruction of the birefringent number '6'. The experimentally measured complex coherence decides the reconstruction quality of the object and the resolution is influenced by the coherence length of the illuminating source at the object plane and also influenced by imaging optics in the Sagnac geometry. We consider that source coherence length is narrower than spatial feature of the object (here number 6) and assumption of delta correlation is considered. Any deviation from the delta correlation feature at the object will influence the resolution and reconstruction quality.

Due to the existing similarity between the optical field and the complex coherence function, the complex CSD matrix elements can be propagated using the angular spectrum method [232]. The propagated source elements at an arbitrary plane z are given by

$$I_{sq}(\mathbf{v}, z;\ \omega) = (\alpha - \alpha^{-1})^2 \int W_{sq}(\alpha^{-1}\boldsymbol{r}, \alpha\boldsymbol{r};\ \omega) \exp\{i[k_z(\alpha\boldsymbol{r};\ \omega) - k_z(\alpha^{-1}\boldsymbol{r};\ \omega)]z\}$$

$$\times \exp[i2\pi(\alpha - \alpha^{-1})(\mathbf{v}.\boldsymbol{r})]\, d^2r \qquad (3.25)$$

Thus, Eq. (3.25) helps to propagate the source digitally at an arbitrary z plane and examine the propagation-induced effects. Fig. 3.8 shows the propagated vector source elements at different z planes for the filtered polarized light from the LED. The first to four rows of Fig. 3.8 represents the different source elements (a)-(e) I_{xx}, (f)-(j) I_{xy}, (k)-(o) I_{yx} and (p)-(t) I_{yy}, respectively. Whereas the first to five columns of Fig. 3.8 shows the propagation of different matrix elements at distances $z = -30mm$, $z = -20mm$, $z = 0$, $z = 20mm$, and $z = 30mm$, respectively. For $z = 0$, the third column of the Fig. 3.8 the focused image of the object and further movement from this plane in either direction results into a defocused image.

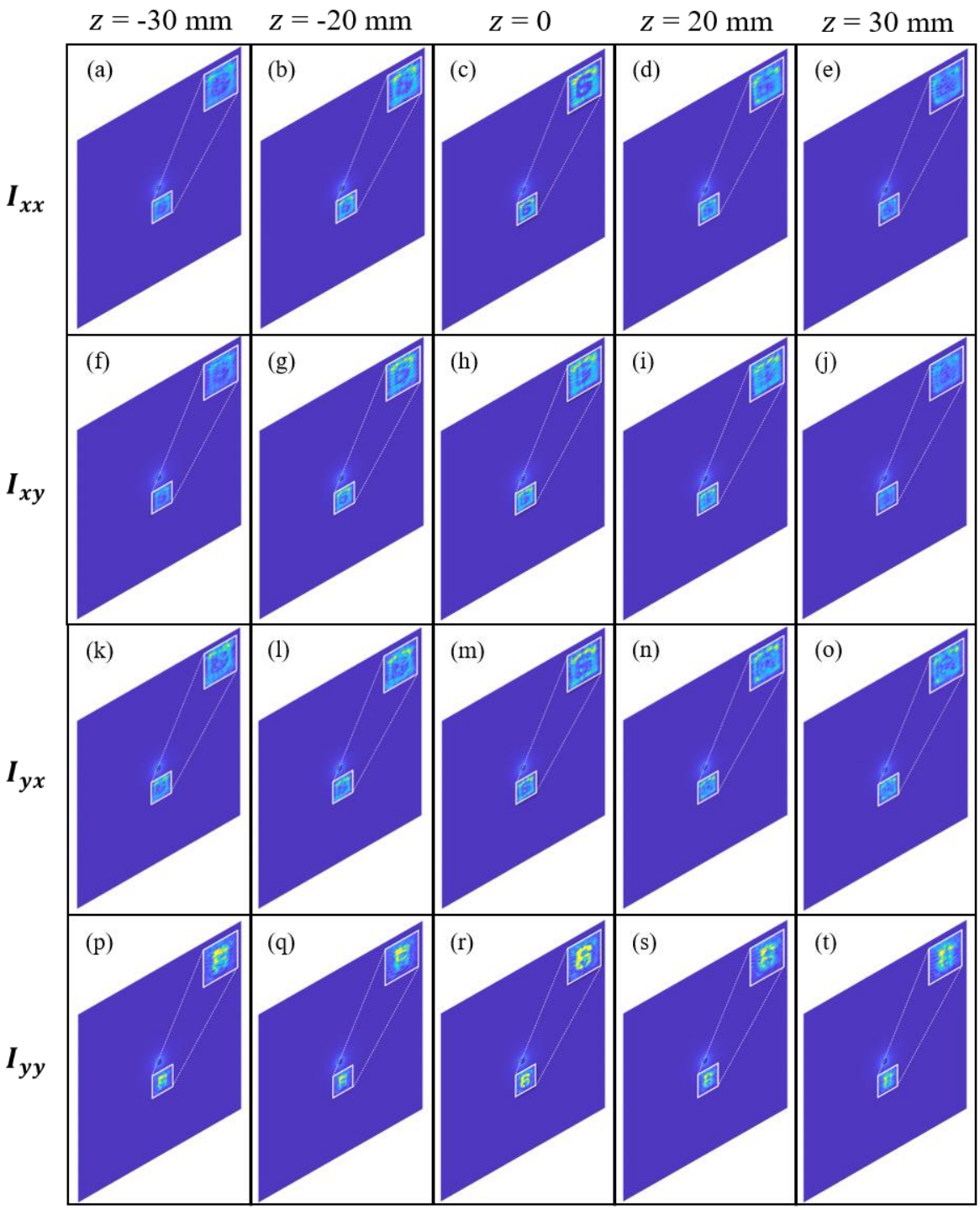

Fig. 3.8 Propagated vector source matrix elements for polarized light: (a)-(e) $\boldsymbol{I_{xx}(r)}$ (f)-(j) $\boldsymbol{I_{xy}(r)}$ (k)-(o) $\boldsymbol{I_{yx}(r)}$ (p)-(t) $\boldsymbol{I_{yy}(r)}$ at different distances $\boldsymbol{z = -30\ mm}$, $\boldsymbol{z = -20\ mm}$, $\boldsymbol{z = 0}$, $\boldsymbol{z = 20\ mm}$ and $\boldsymbol{z = 30\ mm}$.

3.3 Effect of polarization on cross-spectral density matrix

The exploration of light's polarization state encompasses both uniform and non-uniform characteristics. In the case of non-uniform polarization, the polarization state may vary in space over the beam's spatial profile with various features such as periodic variations [268-270], circular symmetry [271], or other complex structures [272-274]. Many intriguing properties have been elucidated for such non-uniformly polarized beams, particularly as they propagate in free space, random media, or through optical systems [192, 275]. Consequently, substantial efforts have been dedicated to comprehensively characterize them and to design and experimentally generate beams with diverse states of coherence and polarization. Here, we analyze the role of source polarization on far-field coherence-polarization of the incoherent source by measuring two-dimensional spatial distributions of the CSD matrix elements. Here, we use a light emitting diode (LED) as an incoherent source and tailored its polarization for two different cases, namely a diagonally-polarized, and a spatially depolarized beam, respectively. Spatial depolarization in the incoherent source is realized by using a double wedge depolarizer (DWD) due to its special polarization features. For comparison of the tailored polarization features of the LED source, we also presented results for unpolarized LED sources. Unlike a point source, LED features an enlarged light-emitting surface. Each point of the extended LED source is acting as an independent light scatterer and there exists no correlation between any two points. Hence, such sources are in general incoherent and with unpolarized light. For the complete analysis of the CSD matrix elements, we built a highly stable Sagnac radial shearing interferometer to measure the second-order field correlations of the vector source. The CSD matrix elements are measured as the complex spatial coherence function, which is obtained from the digitally constructed visibility and phase from the four phase-shifted interferograms. Phase shifts in our experimental configuration are realized by introducing

the geometric phase shifts in the interfering beams [264]. Hence, the study investigates the impact of polarization states of input light on the elements of the CSD matrix. Detailed discussion on the theoretical basis, experimental design, and results are discussed below.

3.3.1 Theoretical basis

Consider a planar, stochastic transverse electromagnetic light beam propagating along the longitudinal z-direction. The second-order statistical characteristics of this stochastic electromagnetic light field, in the space-frequency domain, at an angular frequency ω and two spatial positions, namely, $\boldsymbol{r}_1 = (x_1, y_1)$ and $\boldsymbol{r}_2 = (x_2, y_2)$, is described by the CSD matrix as [2]

$$\mathbf{W}(\boldsymbol{r}_1, \boldsymbol{r}_2; \omega) = \begin{bmatrix} W_{xx}(\boldsymbol{r}_1, \boldsymbol{r}_2; \omega) & W_{xy}(\boldsymbol{r}_1, \boldsymbol{r}_2; \omega) \\ W_{yx}(\boldsymbol{r}_1, \boldsymbol{r}_2; \omega) & W_{yy}(\boldsymbol{r}_1, \boldsymbol{r}_2; \omega) \end{bmatrix}, \tag{3.26}$$

The matrix elements are represented as

$$W_{sq}(\boldsymbol{r}_1, \boldsymbol{r}_2; \omega) = \langle U_s^*(\boldsymbol{r}_1; \omega) U_q(\boldsymbol{r}_2; \omega) \rangle, \tag{3.27}$$

where $(s, q) \equiv (x, y)$ represents the orthogonal polarization components, $U_s(\boldsymbol{r})$ is the fluctuating electric field component at point $\boldsymbol{r}$ along s-axis. The asterisk denotes the complex conjugate and the angle bracket denotes the ensemble average. The individual elements of the 2x2 CSD matrix represent the two-point correlation function between the same field components and the different field components.

From the theory of non-negative kernels, the CSD matrix elements should satisfy the non-negative definiteness condition, and the elements are represented as [259]

$$W_{sq}(\boldsymbol{r}_1, \boldsymbol{r}_2; \omega) = \iint I_{sq}(\mathbf{v}; \omega) H^*(\boldsymbol{r}_1, \mathbf{v}) H(\boldsymbol{r}_2, \mathbf{v}) d^2\mathbf{v}, \tag{3.28}$$

where I_{sq} represents the elements of a 2x2 matrix signifying the polarization through single-point correlation of the incoherent source and H is a propagation kernel which connects the output and input transverse plane coordinates $\boldsymbol{r}$ and $\mathbf{v}$, respectively.

For a Fourier kernel $$H(\boldsymbol{r}, \mathbf{v}) = exp\left(-\frac{i2\pi}{\lambda f}(\boldsymbol{r}.\mathbf{v})\right), \tag{3.29}$$

where λ is the wavelength of the source and f is the focal length of the Fourier transforming lens L.

From Eqns. (3.28) and (3.29), the CSD matrix, of a quasi-monochromatic source, at the observation plane is given by

$$W_{sq}(\boldsymbol{r}_1, \boldsymbol{r}_2) = \int I_{sq}(\mathbf{v})\, exp\left\{-i\frac{2\pi}{\lambda f}[\mathbf{v}.(\boldsymbol{r}_2 - \boldsymbol{r}_1)]\right\} d\mathbf{v}, \tag{3.30}$$

Our specific choice of the Fourier kernel aligns with our goal to analyze the two-point correlations in the far-field from the source. The spatial distribution of the incoherent vector source is represented as $I_{sq}(\mathbf{v})$ and this quantity is real for the diagonal elements, i.e., $s = q$ but may take complex value for the non-diagonal elements, i.e., $s \neq q$. Eq. (3.30) represents the vectorial van Cittert-Zernike (VCZ) theorem; it shows that the elements of the CSD matrix are represented by complex spatial coherence function given by the Fourier transform of the incoherent source. The VCZ theorem establishes a connection between an incoherent source's spatial shape and size and its complex spatial coherence function. Therefore, the complex two-point correlation functions of the vector source at the observation plane relate to the incoherent vector source by the vectorial VCZ theorem [201].

Fig. 3.9 highlights the source structure and far-field configuration of two-point correlations. A yellow light emitting diode (LED) source is kept at the front focal plane of lens L of focal length f = 60 mm. Measurement is performed at the back focal plane of the lens L as represented by the black dotted line in Fig. 3.9. To understand the role of polarization tailoring in the far-field coherence properties of the vector source, we considered three different states of polarization of the incoherent source. These states are unpolarized, diagonally polarized, and spatially depolarized light sources.

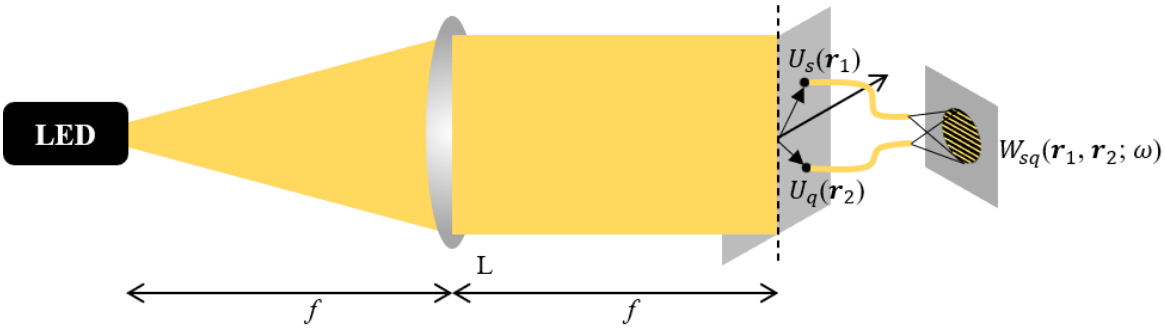

Fig. 3.9 Schematic representation of measurement of two-point correlation in the far-field from an incoherent source, L: Lens.

The first polarization state of the source is realized by directly considering the light from the LED source, as shown in Fig. 3.9. Second polarization state is realized by placing a linear polarizer oriented at 45° from its fast axis after the source in Fig. 3.9. Finally, third polarization state is realized with the DWD (Thorlabs DPU-25-A Quartz-Wedge Achromatic Depolarizer) in the source configuration. The depolarizer, with a thickness of 7.4 mm, contains a broadband anti-reflectance coating that spans from 350 nm to 700 nm. As illustrated in Fig. 3.10, the DWD is comprised of two birefringent quartz wedges (with a wedge angle a = 2.17°) with their optic axes (fast axes) oriented at ξ = 45° relative to each other. The 45° offset lets the plates spatially depolarize the incoming polarization state. A linearly polarized beam along one plate's fast axis will undergo polarization changes due to the birefringence of the other plate. Since the plates are wedged, the optical path length through each birefringent plate varies with the beam's position. Consequently, each point on the aperture exhibits spatially dependent net birefringence and final polarization state [269]. Therefore, DWD introduces a periodic polarization pattern in the source structure. The mathematics underlying this statement is presented in the below equations [197].

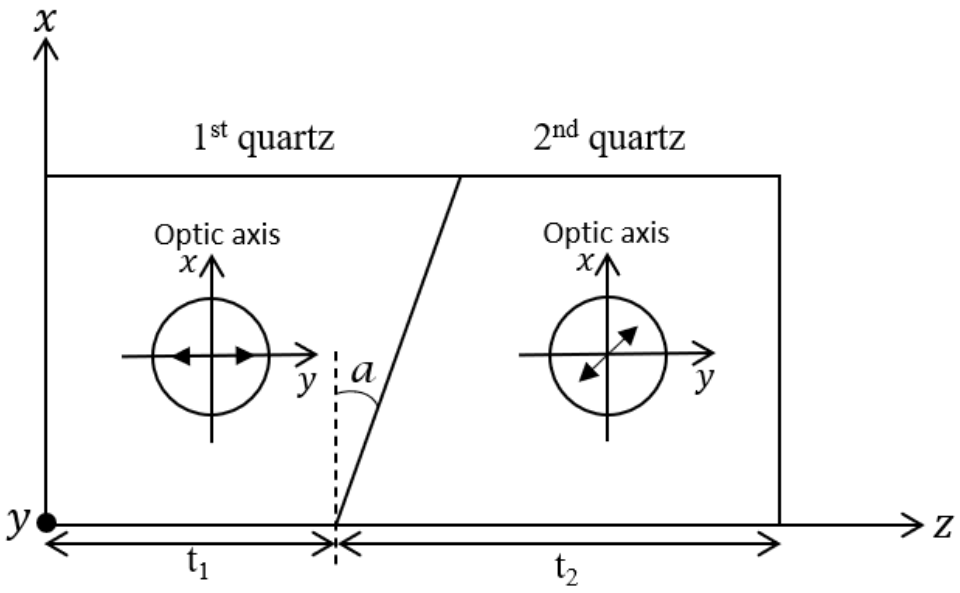

Fig. 3.10 Schematic illustration of a DWD [269].

The DWD is considered as a composition of two wave plates, where the retardation varies with the spatial coordinate x. When the DWD is rotated about the z-axis at an angle χ with respect to the x-axis, thicknesses of the quartz wedges are represented as

$$\mathrm{t'}_1(x) = x \cos\chi \tan a + \mathrm{t}_1, \tag{3.31}$$

and

$$\mathrm{t'}_2(x) = x \cos\chi \tan a + \mathrm{t}_2, \tag{3.32}$$

where t_1 and t_2 are the center thicknesses of the 1st and 2nd quartz wedges, respectively at $x = y = 0$ and a is the wedge angle. Therefore, the wedges retardations are given by

$$\psi_p(x) = 2\pi \mathrm{t'}_p(x)\,(n_s - n_f)/\lambda,\ p \in \{1, 2\}, \tag{3.33}$$

where n_s and n_f are the refractive indices of quartz with respect to the slow and fast axis, respectively. Due to the position-dependent retardation, an input beam with a uniform polarization would result in an output beam with a spatially periodic polarization modulation with period $L = \lambda/[(n_s - n_f)\tan a]$.

The Jones matrix of an individual quartz wedge with its fast axis directed along the x direction is represented as [197]

$$\mathbf{M}_p(x) = \begin{pmatrix} 1 & 0 \\ 0 & exp\left[i\psi_p(x)\right] \end{pmatrix}, \quad p \in \{1,2\}, \tag{3.34}$$

If the optic axis is oriented such that it forms an angle ξ with the x-axis, the Jones matrix is now transformed as

$$\mathbf{M}_p(x\,;\xi_p) = \mathbf{R}(-\xi_p)\mathbf{M}_p(x)\mathbf{R}(\xi_p), \quad p \in \{1,2\}, \tag{3.35}$$

where

$$\mathbf{R}(\xi) = \begin{pmatrix} cos\,\xi & sin\,\xi \\ -sin\,\xi & cos\,\xi \end{pmatrix}, \tag{3.36}$$

$\mathbf{R}(\xi)$ is the rotational matrix that represents the DWD's rotation about the z-axis. The overall matrix of the DWD is finally described as [197]

$$\mathbf{M}_{DWD}(x;\xi_1,\xi_2) = \mathbf{M}_2(x;\xi_2)\mathbf{M}_1(x;\xi_1), \tag{3.37}$$

When the depolarizer is rotated at an angle χ, the resulting matrix becomes

$$\mathbf{M}_{DWD,rot}(x;\xi_1,\xi_2,\chi) = \mathbf{R}(-\chi)\mathbf{M}_{DWD}(x;\xi_1,\xi_2)\mathbf{R}(\chi), \tag{3.38}$$

Thus, at the output plane of DWD, the Jones vector is given by

$$U_{output} \propto \mathbf{M}_{DWD,rot}(x;\xi_1,\xi_2,\chi)U_i, \tag{3.39}$$

where the Jones vector of the incident beam is represented as U_i. As a result, the properties of the DWD produce a periodic polarization modulation at the incoherent source.

3.3.2 Experiment and results discussions

Fig. 3.11 shows the experimental setup to obtain CSD matrix elements. The initial part of the setup corresponds to the schematic depicted in Fig. 3.9. Here, we capture the two-point far-field correlation at the back focal plane of lens L, marked by the black dotted line in Figure 3. Whereas, the second part represents the interferometric design to measure the CSD matrix and provide their two-dimensional distribution at the observation plane. This interferometer uses a cyclic Sagnac geometry with a radial shearing design. The stochastic field from the source is directed into the interferometer by a polarizing beam splitter (PBS). The PBS splits the incoming beam into two beams with orthogonal x and y polarization states. The two beams counter propagate through a square cyclic path designed by mirrors

M1, M2, and M3. The lenses L2 and L3 with focal lengths f_2 = 120 mm and f_3 = 125 mm are introduced in the path of the counter-propagating beams to form a telescopic lens system with magnifications $\alpha = f_3/f_2 = 1.041$ and $\alpha^{-1} = f_2/f_3 = 0.96$, respectively which gives a radial shear between the two beams. Therefore, two copies of the radially sheared fields are obtained at the output of the interferometer. Therefore, the far-field of lens L is imaged onto an 8-bit CMOS camera (Thorlabs DCC3240M). At the imaging plane, the interference pattern at an arbitrary position $\boldsymbol{r}$ arises due to the superposition of the fields from the spatial positions $\boldsymbol{r}_1 = \alpha^{-1}\boldsymbol{r}$ and $\boldsymbol{r}_2 = \alpha\boldsymbol{r}$ of the two copies of the beam. The field points separated by a distance $\Delta\boldsymbol{r} = \boldsymbol{r}_2 - \boldsymbol{r}_1 = (\alpha - \alpha^{-1})\boldsymbol{r}$ represent the relative shear among the two fields, which shows a linear relation between the relative shear $\Delta\boldsymbol{r}$ and the position vector $\boldsymbol{r}$, scaled by factor $(\alpha - \alpha^{-1})$. To reconstruct elements of the CSD matrix, *i.e.*, $W_{sq}(\alpha^{-1}\boldsymbol{r}, \alpha\boldsymbol{r};\ \omega)$, four-step phase shifting approach is implemented.

A combination of quarter waveplate (QWP) and polarizer P3 is kept before the camera introduces phase shifts in the interferometer [264]. The orthogonal linear polarization states x and y at the output are converted to RCP and left circularly polarized LCP states, respectively by a QWP. The polarizer P3 is rotated by an angle θ so that it introduces a phase shift 2θ between the two interfering beams. Four interferograms with phase shifts 0, π/2, π and 3π/2 are recorded.

The fringe visibility, i.e. amplitude of the complex correlation function $g_{sq}(\boldsymbol{r}_1, \boldsymbol{r}_2)$ and its phase $\phi_{sq}(\boldsymbol{r}_1, \boldsymbol{r}_2)$ is constructed using the recorded interferograms as follows

$$g_{sq}(\boldsymbol{r}_1, \boldsymbol{r}_2) \propto \frac{\sqrt{\left[I_{sq}(0) - I_{sq}(\pi)\right]^2 + \left[I_{sq}(\pi/2) - I_{sq}(3\pi/2)\right]^2}}{I_{sq}(0) + I_{sq}(\pi/2) + I_{sq}(\pi) + I_{sq}(3\pi/2)}, \tag{3.40}$$

$$\phi_{sq}(\boldsymbol{r}_1, \boldsymbol{r}_2) = tan^{-1}\left[\frac{I_{sq}(3\pi/2) - I_{sq}(\pi/2)}{I_{sq}(\pi) - I_{sq}(0)}\right], \tag{3.41}$$

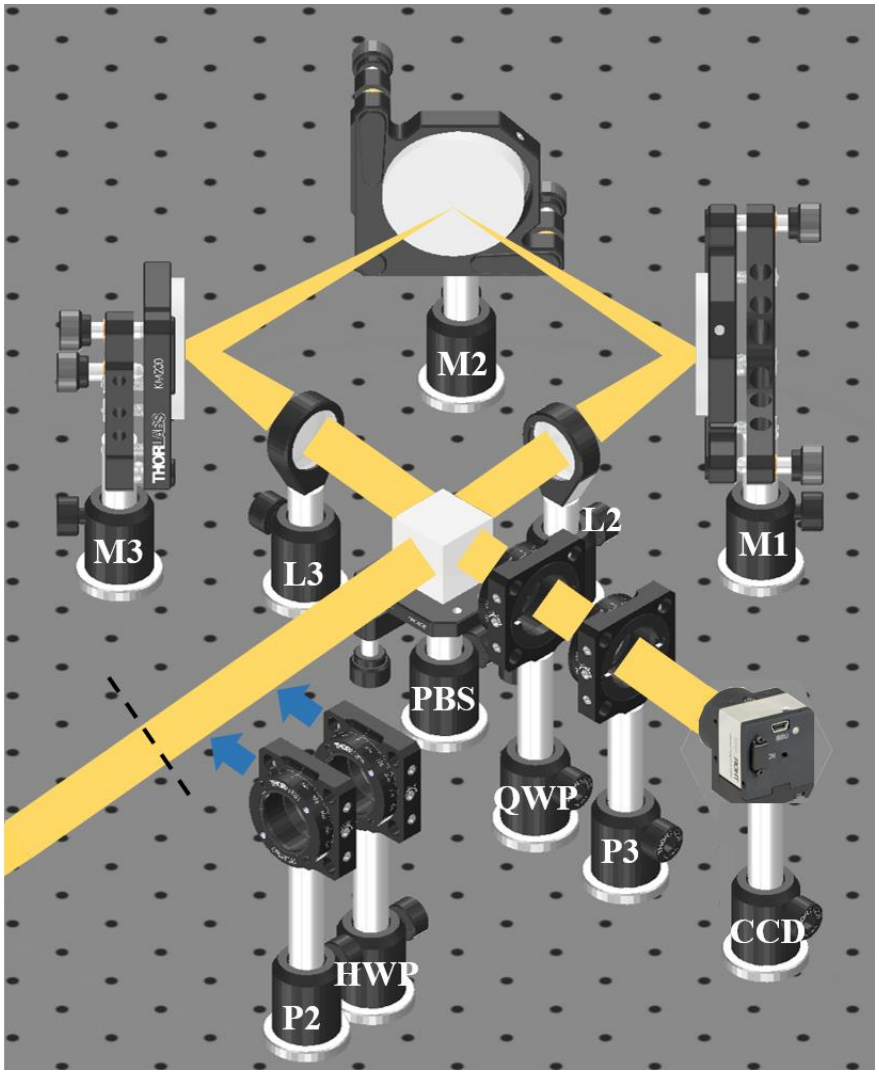

Fig. 3.11 Experimental setup Square Sagnac Radial Shearing Interferometer: P: Polarizer, DWD: Double Wedge Depolarizer, L: Lens, PBS: Polarization Beam Splitter, M: Mirror, HWP: Half Wave Plate, QWP: Quarter Wave Plate, CCD: Charge-Coupled Device.

Eq. (3.40) and Eq. (3.41), provide the amplitude and phase of the complex two-point correlation function, respectively. Subsequently, we reconstruct the two-point correlation elements of the CSD matrix as follows

$$W_{sq}(\alpha^{-1}\boldsymbol{r}, \alpha\boldsymbol{r}) = g_{sq}(\alpha^{-1}\boldsymbol{r}, \alpha\boldsymbol{r})\, exp\big[i\phi_{sq}(\alpha^{-1}\boldsymbol{r}, \alpha\boldsymbol{r})\big], \tag{3.42}$$

where $\alpha^{-1}\boldsymbol{r} = \boldsymbol{r}_1$ and $\alpha\boldsymbol{r} = \boldsymbol{r}_2$.

The experimental setup in Fig. 3.11 provides 2D distribution of the $W_{xy}(\alpha^{-1}\boldsymbol{r}, \alpha\boldsymbol{r})$ without scanning and offers an effective and fast method to evaluate the complex two-point correlation function. To measure $W_{xx}(\alpha^{-1}\boldsymbol{r}, \alpha\boldsymbol{r})$, the polarizer P2 is rotated such that it

selects only x-polarized component from the diagonally polarized beam. Similarly, to measure $W_{yy}(\alpha^{-1}\boldsymbol{r}, \alpha\boldsymbol{r})$, the polarizer P2 is rotated such that it selects only y-polarized component from the diagonally polarized beam. Later, a HWP is inserted and oriented at an angle 22.5˚ from its fast axis (along the x direction) to equal the intensities in the two arms of the interferometer. Again, following the same previously described process we recorded the four interferograms for $W_{xx}(\alpha^{-1}\boldsymbol{r}, \alpha\boldsymbol{r})$ and $W_{yy}(\alpha^{-1}\boldsymbol{r}, \alpha\boldsymbol{r})$, respectively. At last, to measure $W_{yx}(\alpha^{-1}\boldsymbol{r}, \alpha\boldsymbol{r})$, only a HWP is inserted before PBS and it is oriented at 45˚ from its fast axis (along the x direction), such that it flips the polarization in the two arms of the interferometer from x to y and y to x component, respectively. The four interferograms are recorded for $W_{yx}(\alpha^{-1}\boldsymbol{r}, \alpha\boldsymbol{r})$ following the formerly described method. It must be noted that the Sagnac radial shearing interferometer being common path, in the measurement of vector components of coherence function at different times, the phase relations are not affected by surrounding vibrations. In addition, the common path geometry ensures that the temporal coherence is sufficiently maintained during the measurement of spatial coherence function even for a finite spatial coherence length (shear along x or y).

Fig. 3.12 shows the recorded interferograms $I_{xy}(0)$, $I_{xy}(\pi/2)$, $I_{xy}(\pi)$ and $I_{xy}(3\pi/2)$ with phase shifts 0, $\pi/2$, π, and $3\pi/2$, respectively corresponding to $W_{xy}(\alpha^{-1}\boldsymbol{r}, \alpha\boldsymbol{r})$ for all three different polarization states of the source, (a1) - (d1) show interferograms for unpolarized LED source, (a2)-(d2) show interferograms for diagonally polarized polarizer and (a3)-(d3) show interferograms for incoherent source with the DWD. These results clearly distinguish the difference between the recorded interferograms for varying polarization states of the incoherent source. The first row of Fig. 3.12 presents results for an unpolarized LED source, revealing the absence of fringes in the captured interferograms. This occurs due to the lack of correlation between the orthogonally polarized field components of un-polarized light. Whereas the second row of Fig. 3.12 shows results for a diagonally polarized light source.

For the vectorial source, modulation in the central part is clearly visible in interferograms for different phase shifts. The last row of the Fig. 3.12 shows the interferograms for a LED source with the DWD. The recorded interferogram shows a periodic pattern and this spatially induced periodic pattern is due to the special properties of DWD as discussed in section 2. Similarly, we have recorded the interferograms for $W_{xx}(\alpha^{-1}\boldsymbol{r}, \alpha\boldsymbol{r})$, $W_{yx}(\alpha^{-1}\boldsymbol{r}, \alpha\boldsymbol{r})$ and $W_{yy}(\alpha^{-1}\boldsymbol{r}, \alpha\boldsymbol{r})$ for all the three different sources, as discussed previously. After recording all four sets of interferograms for four elements of the CSD matrix, we experimentally recovered the complex elements of the CSD matrix for different cases using Eqns. (3.40) - (3.42).

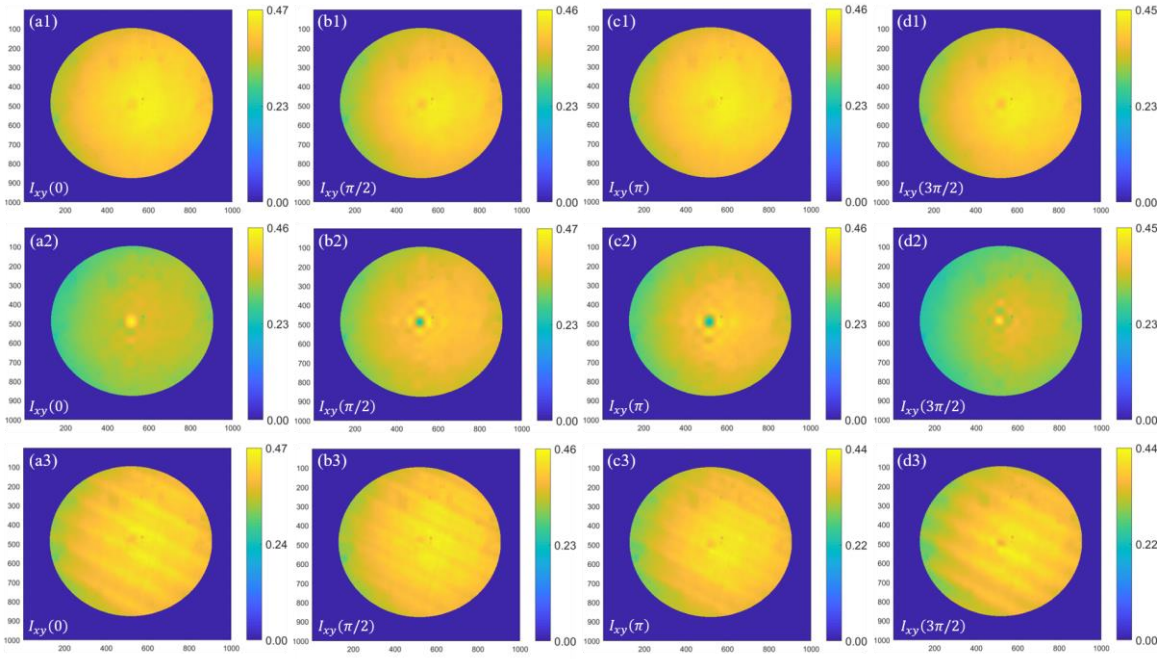

Fig. 3.12 Four experimentally recorded interferograms for phase-shifts 0, π/2, π, and 3π/2 for $\boldsymbol{W_{xy}(\alpha^{-1}r, \alpha r)}$ (a1) - (d1) unpolarized LED (a2) - (d2) diagonally polarized polarizer (a3) - (d3) DWD.

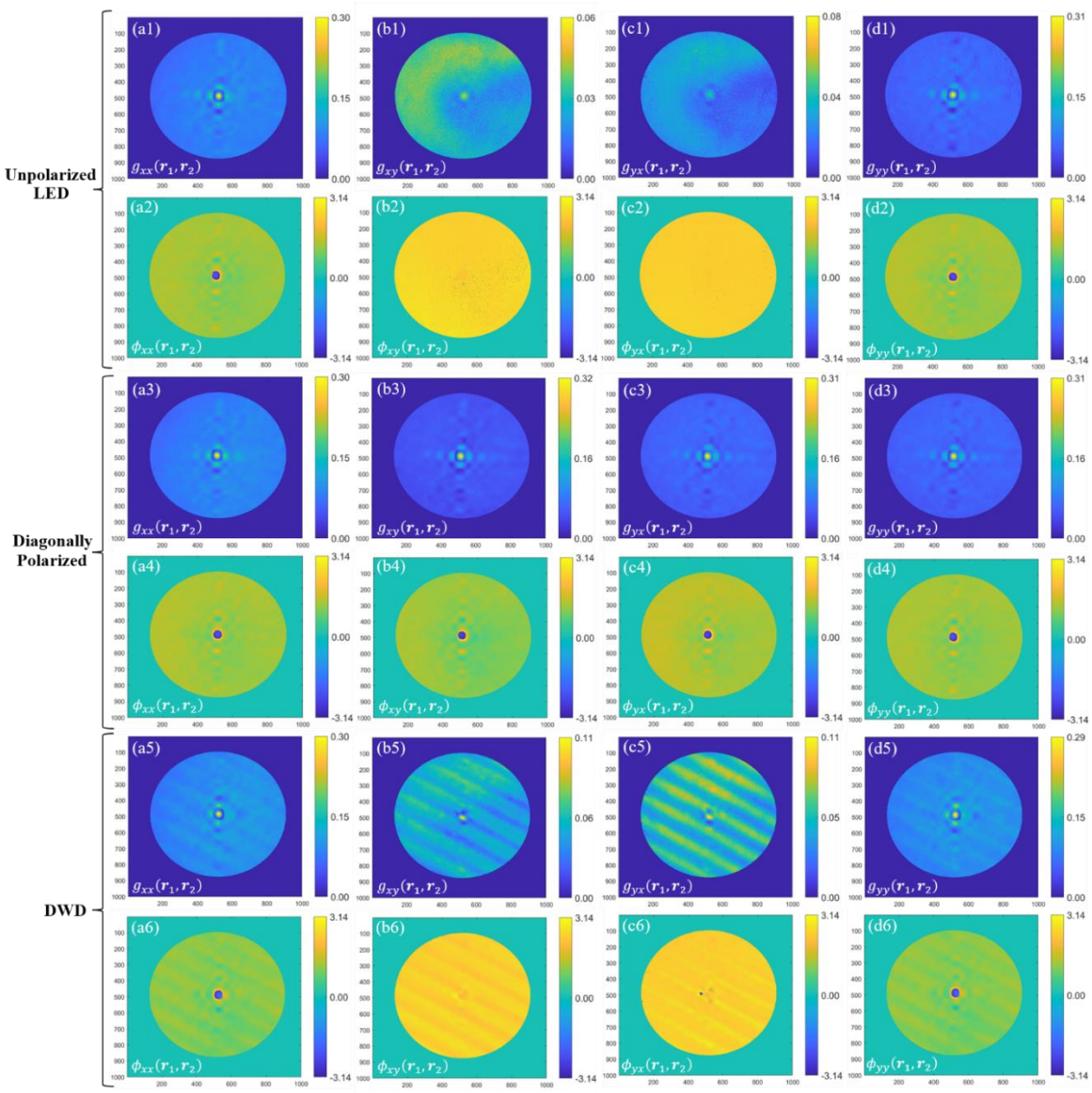

Fig. 3.13 Elements of CSD matrix for three different cases (a1) - (d2) unpolarized LED, (a3) - (d4) diagonally polarized polarizer, and (a5) - (d6) DWD. In different sets, the absolute value of CSD matrix elements *i.e.* fringe visibility values are represented using $\boldsymbol{g_{sq}(r_1, r_2)}$, and the corresponding phases using $\boldsymbol{\phi_{sq}(r_1, r_2)}$.

Fig. 3.13 shows the results of amplitude (fringe visibility) and corresponding phase of the CSD matrix elements using Eqns. (3.40) and (3.41) for three sources namely unpolarized LED, diagonally polarized LED light, and polarization tailored by the DWD. Fig. 3.13 (a1) - (d1) shows the experimentally recorded amplitude and (a2) - (d2) corresponding phases for CSD matrix elements of the unpolarized LED source. Fig. 3.13 (a1) shows the amplitude and (a2) corresponding phase for $W_{xx}(\alpha^{-1}\boldsymbol{r}, \alpha\boldsymbol{r})$. The observed result shows the

presence of fringe visibility for the unpolarized LED light because of the existing correlation between similar polarization components. In Fig. 3.13 (a1), the colormap illustrates that the maximum value of the correlation reaches 0.30. Whereas Fig. 3.13 (a2) shows the phase variation ranging from $-\pi$ to π. Fig. 3.13 (b1) shows the amplitude and (b2) corresponding phase for $W_{xy}(\alpha^{-1}\boldsymbol{r}, \alpha\boldsymbol{r})$ and Fig. 3.13 (b2) shows the amplitude and (c2) corresponding phase for $W_{yx}(\alpha^{-1}\boldsymbol{r}, \alpha\boldsymbol{r})$. Negligible amplitude of $W_{xy}(\alpha^{-1}\boldsymbol{r}, \alpha\boldsymbol{r})$ and $W_{yx}(\alpha^{-1}\boldsymbol{r}, \alpha\boldsymbol{r})$ emerges due to lack of correlations among the orthogonal polarization components in the unpolarized LED source. Fig. 3.13 (d1) shows the amplitude and (d2) phase for $W_{yy}(\alpha^{-1}\boldsymbol{r}, \alpha\boldsymbol{r})$. The results reveal fringe visibility arising from the existing correlation among similar polarization components. The colormap in Fig. 3.13 (d1) shows that the maximum value of the fringe visibility approaches 0.31. The third and fourth row in Fig. 3.13 shows the results for a diagonally polarized light after filtering from the LED. Fig. 3.13 (a3) - (d3) shows amplitude and (a4) - (d4) shows the corresponding phase of $W_{xx}(\alpha^{-1}\boldsymbol{r}, \alpha\boldsymbol{r})$, $W_{xy}(\alpha^{-1}\boldsymbol{r}, \alpha\boldsymbol{r})$, $W_{yx}(\alpha^{-1}\boldsymbol{r}, \alpha\boldsymbol{r})$ and $W_{yy}(\alpha^{-1}\boldsymbol{r}, \alpha\boldsymbol{r})$, respectively. The existence of fringes in all CSD matrix elements is attributed to the polarization filtering of the source by a linear polarizer oriented at 45° from its fast axis after the source. The maximum value for fringe visibility is around 0.31 and the phase map shows variation in range of $-\pi$ to π. The fifth and sixth row in Fig. 3.13 shows the experimental results for the LED source with a DWD. Fig. 3.13 (a5) - (d5) shows amplitude and (a6) - (d6) shows the corresponding phase of $W_{xx}(\alpha^{-1}\boldsymbol{r}, \alpha\boldsymbol{r})$, $W_{xy}(\alpha^{-1}\boldsymbol{r}, \alpha\boldsymbol{r})$, $W_{yx}(\alpha^{-1}\boldsymbol{r}, \alpha\boldsymbol{r})$ and $W_{yy}(\alpha^{-1}\boldsymbol{r}, \alpha\boldsymbol{r})$, respectively. A periodic pattern is evident in the elements of the CSD matrix, attributed to the properties of DWD. Fig. 3.13 (a5) and (d5) show the amplitude of $W_{xx}(\alpha^{-1}\boldsymbol{r}, \alpha\boldsymbol{r})$ and $W_{yy}(\alpha^{-1}\boldsymbol{r}, \alpha\boldsymbol{r})$, respectively. Fig. 3.13 (a6) and (d6) show the corresponding phase of $W_{xx}(\alpha^{-1}\boldsymbol{r}, \alpha\boldsymbol{r})$ and $W_{yy}(\alpha^{-1}\boldsymbol{r}, \alpha\boldsymbol{r})$, respectively. Whereas, Fig. 3.13 (b5) and (c5) show amplitude of $W_{xy}(\alpha^{-1}\boldsymbol{r}, \alpha\boldsymbol{r})$ and $W_{yx}(\alpha^{-1}\boldsymbol{r}, \alpha\boldsymbol{r})$, respectively.

Similarly, the corresponding phase Fig. 3.13 (b6) and (c6) for $W_{xy}(\alpha^{-1}\boldsymbol{r}, \alpha\boldsymbol{r})$ and $W_{yx}(\alpha^{-1}\boldsymbol{r}, \alpha\boldsymbol{r})$, respectively shows a regular periodic variation**.** The DWD's periodic modulation appears in the CSD matrix, demonstrating that the spatial structure is preserved in the far field. Diagonal elements (W_{xx}, W_{yy}) show amplitude modulation due to polarization scrambling and auto-correlation between same polarization components. Off-diagonal elements (W_{xy}, W_{yx}) reveal phase periodicity from the DWD's birefringence and cross-correlation between different polarization components. Therefore, the CSD matrix elements are measured point-by-point via interferometry, capturing the full 2D spatial dependence of polarization. No averaging is applied—each pixel's fringe visibility and phase reflect local polarization states. Therefore, influence of polarization appears in the elements of the CSD matrix.

3.4 Conclusion

This chapter introduced an innovative experimental approach for measuring the two-dimensional structures of the CSD matrix elements. The technique uses a common-path Sagnac radial shearing interferometer integrated with a phase-shifting method. The principle underlying the approach is thoroughly explained and successfully demonstrated through experimental implementation. The method facilitates recording incoherent vector holograms, from which fringe visibility and phase information are extracted to construct the complex CSD matrix elements. Additionally, the approach is applied to analyze the effect of polarization on the CSD matrix elements, providing insights into the interaction between coherence and polarization. This experimental framework holds significant potential for characterizing coherence-polarization properties of light and advancing imaging techniques that leverage stochastic vector light sources.